

# Formation, vertex deviation and age of the Milky Way’s bulge: input from a cosmological simulation with a late-forming bar

Victor P. Debattista<sup>1\*</sup>, Oscar A. Gonzalez<sup>2</sup>, Robyn E. Sanderson<sup>3</sup>,  
Kareem El-Badry<sup>4</sup>, Shea Garrison-Kimmel<sup>3†</sup>, Andrew Wetzel<sup>5</sup>,  
Claude-André Faucher-Giguère<sup>6</sup>, Philip F. Hopkins<sup>3</sup>

<sup>1</sup> *Jeremiah Horrocks Institute, University of Central Lancashire, Preston, PR1 2HE, UK*

<sup>2</sup> *UK Astronomy Technology Centre, Royal Observatory, Blackford Hill, Edinburgh EH9 3HJ, UK*

<sup>3</sup> *TAPIR, MC 350-17, California Institute of Technology, Pasadena, CA 91125, USA*

<sup>4</sup> *Department of Astronomy and Theoretical Astrophysics Center, University of California Berkeley, Berkeley, CA 94720*

<sup>5</sup> *Department of Physics, University of California, Davis, CA 95616, USA*

<sup>6</sup> *Department of Physics and Astronomy and Center for Interdisciplinary Exploration and Research in Astrophysics (CIERA), Northwestern University, 2145 Sheridan Road, Evanston, IL 60208, USA*

*Draft version on 10 April 2019*

## ABSTRACT

We present the late-time evolution of `m12m`, a cosmological simulation of a Milky Way-like galaxy from the FIRE project. The simulation forms a bar after redshift  $z = 0.2$ . We show that the evolution of the model exhibits behaviours typical of *kinematic fractionation*, with a bar weaker in older populations, an X-shape traced by the younger, metal-rich populations and a prominent X-shape in the edge-on mean metallicity map. Because of the late formation of the bar in `m12m`, stars forming after 10 Gyr ( $z = 0.34$ ) significantly contaminate the bulge, at a level higher than is observed at high latitudes in the Milky Way, implying that its bar cannot have formed as late as in `m12m`. We also study the model’s vertex deviation of the velocity ellipsoid as a function of stellar metallicity and age in the equivalent of Baade’s Window. The formation of the bar leads to a non-zero vertex deviation. We find that metal-rich stars have a large vertex deviation ( $\sim 40^\circ$ ), which becomes negligible for metal-poor stars, a trend also found in the Milky Way, despite not matching in detail. We demonstrate that the vertex deviation also varies with stellar age and is large for stars as old as 9 Gyr, while 13 Gyr old stars have negligible vertex deviation. When we exclude stars that have been accreted, the vertex deviation is not significantly changed, demonstrating that the observed variation of vertex deviation with metallicity is not necessarily due to an accreted population.

**Key words:** Galaxy: bulge – Galaxy: evolution – Galaxy: formation – Galaxy: kinematics and dynamics – Galaxy: structure

## 1 INTRODUCTION

Our understanding of the formation of the bulge of the Milky Way (MW) has advanced considerably, with large new observational surveys (e.g. Howard et al. 2008; Freeman et al. 2013; Saito et al. 2012; Zoccali et al. 2014; Majewski et al. 2016; Ness et al. 2012), careful comparison with simulations (e.g. Shen et al. 2010; Martinez-Valpuesta & Gerhard 2011,

2013; Di Matteo et al. 2015; Di Matteo 2016; Debattista et al. 2017; Athanassoula et al. 2017; Fragkoudi et al. 2017b, 2018; Buck et al. 2018b,a), and detailed dynamical models of its current state (e.g. Bissantz et al. 2004; Portail et al. 2015, 2017). All three approaches have now deconstructed the bulge by stellar populations, demonstrating how its properties vary as a function of metallicity (Ness et al. 2013; Di Matteo et al. 2015; Debattista et al. 2017; Portail et al. 2017; Athanassoula et al. 2017; Fragkoudi et al. 2018). Multiple studies have converged to the conclusion that the majority of the bulge formed purely from the secular evolution of the

\* E-mail: vpdebattista@gmail.com

† Einstein Fellow

disc, via the bar that forms within it. Based on the kinematics of M-giants observed in BRAVA (Howard et al. 2008), Shen et al. (2010) estimated that any accreted component constitutes less than 8% of the stellar mass of the MW, while Debattista et al. (2017) showed that the presence of a hot component only becomes evident at low metallicities, where the addition of 1.3% of the total stellar mass in kinematically hot stars is sufficient to match the kinematics of these stars. In a similar vein Di Matteo et al. (2014) estimated that a classical bulge with 25% of the disc mass can be excluded. Bonaca et al. (2017) and El-Badry et al. (2018a) showed that the kinematics of old, accreted, metal-poor stars in the central spheroid are indistinguishable from those of the stars of the same age that formed in situ. Therefore the observed population of kinematically hot stars must include stars that formed in situ, making the contribution of an accreted population even lower. Properties that the secular evolution model can now account for include the vertical metallicity gradient, the predominantly old stars in the bulge, the age and metallicity variation of the X-shape and bar strength, and the different kinematics of stars of different age. The key mechanism driving the observed trends with stellar populations is the separation of stellar populations by an evolving bar on the basis of their radial velocity dispersions, a process termed *kinematic fractionation* by Debattista et al. (2017). This occurs because kinematically hot populations have a lower angular frequency relative to the bar. The frequency at which they encounter a vertical bend in the bar is therefore lower than for a cool population, allowing them to be pumped by the bar to larger heights before their response to the forcing is out of phase (Merritt & Sellwood 1994). Since stellar populations typically get kinematically hotter as they age, kinematic fractionation generally results in a continuum of properties as a function of age. Starting with Bekki & Tsujimoto (2011), and subsequently Di Matteo (2016) and Fragkoudi et al. (2017a) reached a similar conclusion using simulations composed of distinct thin and thick discs. While stars in the simulation of Debattista et al. (2017) all form self-consistently from gas, the simulation was evolved in isolation, removed from a larger scale cosmological context. Recently Buck et al. (2018b) demonstrated that the signatures of kinematic fractionation also occur in a cosmological simulation. Here we confirm this result using a cosmological simulation, **m12m**, from the Feedback In Realistic Environments (FIRE) project.

One of the properties of the bulge which is yet to be explained without invoking an accreted population is the absence of a significant vertex deviation in the most metal-poor stars of the bulge (Soto et al. 2007; Babusiaux et al. 2010). The vertex deviation measures the covariance between radial and tangential motions (from the Sun’s point of view). A stationary, axisymmetric disc has no vertex deviation, whereas a triaxial bar necessarily introduces a vertex deviation (Binney & Tremaine 2008). Observations show that the metal-rich stars in Baade’s Window ( $(l, b) = (1^\circ, -4^\circ)$ ) have a significant vertex deviation, while the metal-poor stars do not. This has often been interpreted as the signature of a separate component in the bulge (e.g. Noguchi 1999; Aguerri et al. 2001). However Debattista et al. (2017) showed that, in their simulation which did not have *any* accreted population, the oldest population hosts a substantially weaker bar than the rest of the stars. Here we explore whether the

vanishing vertex deviation of old stars depends upon the formation location (in-situ versus accreted).

A further uncertainty about the MW’s bar is its age. Since a bar is formed from stars in the disc, a bar will always contain stars older than itself. But the bar also grows over time, by shedding angular momentum (e.g. Weinberg 1985; Debattista & Sellwood 2000; Athanassoula 2002; O’Neill & Dubinski 2003; Martinez-Valpuesta et al. 2006), with the possibility of trapping stars that are younger than the bar itself (e.g. Aumer & Schönrich 2015). Therefore measuring the age of the MW’s bar is difficult. Studies of the age distribution of stars in the bulge have generally found old stars (Ortolani et al. 1995; Kuijken & Rich 2002; Zoccali et al. 2003; Sahu et al. 2006; Clarkson et al. 2008, 2011; Brown et al. 2010; Valenti et al. 2013; Calamida et al. 2014). In contrast, spectroscopy of microlensed dwarfs has found a wide range of stellar ages in the bulge, including very young stars at high metallicity (Bensby et al. 2011, 2013, 2017). More recently, Haywood et al. (2016) have proposed that the bulge hosts stars between 13 Gyr and 3 Gyr old to explain the narrow range of turnoffs. Bernard et al. (2018) found that over 80% of stars on the bar’s minor axis are older than 8 Gyr but that a significant fraction of super-solar metallicity stars are younger and that 11% of all stars on the minor axis are younger than 5 Gyr. All these studies agree that young stars are predominantly or exclusively found at high metallicities and, therefore, not expected to be found at high Galactic latitudes, where low metallicity stars dominate (e.g. Zoccali et al. 2017). These studies however have not provided constraints on the age of the bar. Alternatively, Buck et al. (2018b) propose that the variation of the X-shape as a function of age can be used to determine the age of the bar. Here we show what the consequences for stellar populations on the minor axis would be if the bar is as young as 2 – 3 Gyr.

This paper is organised as follows. Section 2 describes the simulation we use. This is followed in Section 3 by several lines of evidence that the bar in this simulation drives kinematic fractionation. Section 4 examines the vertex deviation of the model, to test whether in-situ populations can have negligible vertex deviation. Section 5 derives constraints on the age of the MW’s bar. We conclude in Section 6.

## 2 SIMULATION

The simulation analyzed in this paper, referred to as **m12m**, is part of the Feedback In Realistic Environments (FIRE)<sup>1</sup> project, specifically the “FIRE-2” version of the code; all details of the methods are described in Hopkins et al. (2018), Section 2. The simulations use the code GIZMO (Hopkins 2015)<sup>2</sup>, with hydrodynamics solved using the mesh-free Lagrangian Godunov “MFM” method. Both hydrodynamic and gravitational (force-softening) spatial resolution are set in a fully-adaptive Lagrangian manner for gas (but not for stars and dark matter). The simulation includes cooling and heating from a meta-galactic background and local stellar sources from  $T \sim 10 - 10^{10}$  K, star formation in locally self-gravitating, dense molecular gas, and stellar feedback from

<sup>1</sup> fire.northwestern.edu

<sup>2</sup> tapir.caltech.edu/~phopkins/Site/GIZMO.html

stars, including stellar winds from O, B and AGB stars, SNe Ia and II, and multi-wavelength photo-heating and radiation pressure, with inputs taken directly from stellar evolution models. The FIRE physics, source code, and all numerical parameters are identical to those described in Hopkins et al. (2018). The basic characteristics of **m12m** are given in Table 1. Of interest for this work is that, like the MW, this simulated galaxy has a strong bar and X-shaped bulge at redshift  $z = 0$  (Figure 1). A movie showing the time-evolution of **m12m** from  $z \sim 8$  to the present day<sup>3</sup> shows that although **m12m** has a turbulent early merger history, including a nearly equal-mass merger at  $z \sim 1.5$  ( $t \sim 4.3$  Gyr), it is relatively peaceful at late times, with only minor mergers since at least  $z \sim 0.5$ . While **m12m** has a satellite mass function similar to that of M31 (Garrison-Kimmel et al. 2018a), interactions are not necessarily the cause of bar formation (see also Zana et al. 2018).

To analyze the structure of **m12m**, the simulation was first centered on the host galaxy by iteratively calculating the *stellar* center of mass. The galaxy is then aligned by calculating the moment of inertia tensor for all stars within 20 kpc of the center, and rotated so that the principal axes of this tensor lie along the three Cartesian axes, with the  $X$  direction pointing along the longest axis and the  $Z$  direction pointing along the shortest axis. Since **m12m** has a well-defined stellar disc, this has the effect of aligning the disc with the  $X$ – $Y$  plane, and the  $Z$  coordinate indicating height above the disc plane. In this coordinate system, stars with height  $|Z| < 10$  kpc and cylindrical radius  $R < 30$  kpc, are selected for analysis. We post-process the snapshots to record the positions of star particles, relative to the host galaxy center at that time, in the first snapshot in which they appear. Since the average time between snapshots is  $\sim 25$  Myr we can refer to this quantity as the “formation distance” of the star particle without much loss of fidelity. In summary, the analysis in this work uses the disc-aligned coordinates, IMF-averaged metallicities, ages, and formation distances of the selected stars.

As discussed in Wetzell et al. (2016), Hopkins et al. (2018), Garrison-Kimmel et al. (2018b), Sanderson et al. (2018) and El-Badry et al. (2018b), **m12m** and the other MW analogs simulated in this mass range with FIRE-2, have stellar-to-halo mass ratios and disc properties resembling those of the MW and M31. In particular **m12m** has a thin gas disc and a double-exponential stellar disc with comparable scale heights to the MW at  $z = 0$  (see Table 1). At the present day **m12m** has about twice the stellar mass of the MW. It also has a much higher star formation rate, even though about 50% of its total stellar mass is in a dispersion-supported system with the rest in a rotationally-supported disc (Garrison-Kimmel et al. 2018b), which is a significantly higher dispersion-supported fraction than in the MW (Bland-Hawthorn & Gerhard 2016). The structure of the disc, bar, and bulge in **m12m** are emergent properties of the simulation, not the result of tuned initial conditions. Thus we can confirm that triaxial structures in the inner regions of galaxies can arise in a fully cosmological formation scenario including filamentary accretion, the response of a cold dark matter halo, and stellar feedback, though we cau-

tion that AGN feedback is not included in this simulation. This is in good agreement with previous results from cosmological simulations (Romano-Díaz et al. 2008; Scannapieco & Athanassoula 2012; Kraljic et al. 2012; Goz et al. 2015; Fiacconi et al. 2015; Okamoto et al. 2015; Bonoli et al. 2016; Spinoso et al. 2017; Buck et al. 2018b).

## 2.1 Simulation scaling

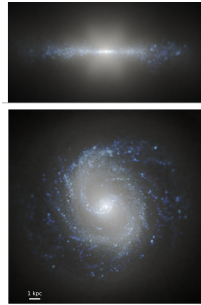
**m12m** has a bar of semi-major axis  $a_B \simeq 6$  kpc. Through most of the paper we present **m12m** without rescaling it. However, studying the vertex deviation and the age distribution requires **m12m** to be scaled in size such that the vertical structure is comparable to that in the MW. We do this by placing the arms of the X-shape in **m12m** at  $z = 0$ , as traced by the peaks in the line-of-sight density distribution, at a comparable location as in the MW. We compute the factor required to obtain a half-length of  $\sim 2$  kpc for the X-shaped bulge in **m12m**. We find that a factor of 0.5, applied to all particles, accomplishes this and results in the arms of the X-shaped bulge having a similar size to those of the MW bulge as mapped by Wegg & Gerhard (2013). To further ensure that this scaling is suitable for comparing **m12m** to the MW, we measure the distance distribution of all stars along the minor axis at different latitudes to identify the Galactic latitude at which the split in distance distributions is first identified. We find that when using a scaling factor of 0.5 the split is first seen at a latitude of  $b \sim 5^\circ$ , which compares well with the MW’s bulge (c.f. McWilliam & Zoccali 2010). The Sun is then placed at 8 kpc from the Galactic centre and the bar is rotated to an angle of  $27^\circ$  with respect to the Galactic centre–Sun line of sight.

We apply no scaling to the velocities because none are needed for our analysis; for the vertex deviation analysis, we are only interested in ratios of dispersions, which do not require the model to be kinematically scaled to the MW. We present maps of the mean velocity and velocity dispersion along the line of sight in Galactic coordinates in Fig. 2. The kinematic maps show a (close-to) cylindrical rotation and a clear peak in velocity dispersion in the central regions that appears vertically elongated. These properties are in good qualitative (but not quantitative) agreement with the ones observed in the MW (Zoccali et al. 2014; Ness et al. 2016), in simulations (Qin et al. 2015; Fragkoudi et al. 2017a; Buck et al. 2018b), and in similar external galaxies (Gonzalez et al. 2016; Molaeinezhad et al. 2016). In particular, the vertically elongated velocity dispersion ‘peak’ presented in Zoccali et al. (2014) is clearly observed in the simulation once it is rescaled.

## 2.2 Star formation history and chemistry

The top panel of Fig. 3 shows the star formation history of the model. Star formation is initially very low, peaking at around 8 Gyr. The star formation rate of the accreted component (not shown) peaks at  $\sim 3$  Gyr, at which time it accounts for  $\sim 40\%$  of the total star formation rate; essentially no star formation occurs after 4 Gyr in the accreted component. By  $t \sim 9$  Gyr the star formation rate has dropped by roughly a factor of two. A second drop, again by a factor of two, in the star formation rate occurs shortly before  $t = 12$  Gyr.

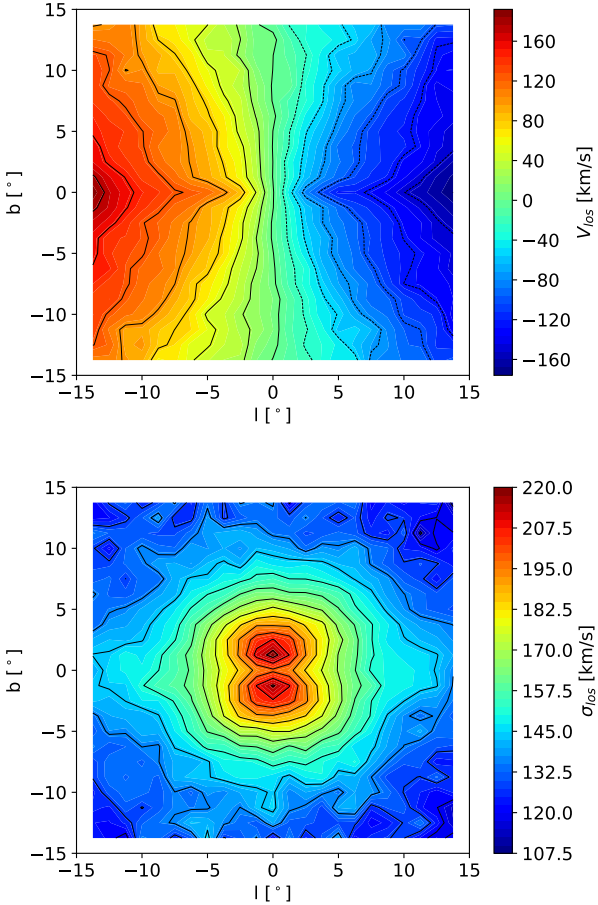
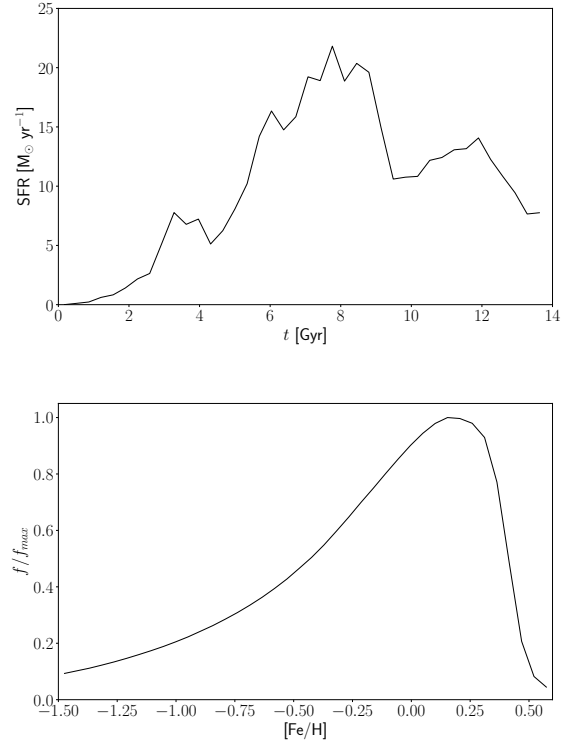
<sup>3</sup> [tapir.caltech.edu/~sheagk/movies/stars/m12m\\_ref13\\_star.mp4](http://tapir.caltech.edu/~sheagk/movies/stars/m12m_ref13_star.mp4)



**Figure 1.** Edge-on (top) and face-on (bottom) views of *m12m* at  $z = 0$ . Each image is a *u/g/r* composite (in *Hubble Space Telescope* bands) with a logarithmic stretch, using STARBURST99 (Leitherer et al. 1999) to determine the spectral energy distribution of each star particle based on its age and metallicity and ray-tracing following Hopkins et al. (2005). To help reveal the structure of the bar, no dust extinction is included. The face-on view shows the central bar, while the edge-on view exhibits a clear X-shape.

**Table 1.** Structural properties of m12m.

Property	Value	Unit
$M_h$ (halo mass at $z = 0$ ; Bryan & Norman (1998))	$1.6 \times 10^{12}$	$M_\odot$
$M_*$ (stellar mass at $z = 0$ )	$1.1 \times 10^{11}$	$M_\odot$
$M_{\text{gas}}$ (gas mass at $z = 0$ )	$1.4 \times 10^{10}$	$M_\odot$
Baryon particle mass	7070	$M_\odot$
Dark matter particle mass	$3.52 \times 10^4$	$M_\odot$
Dark matter softening length	40	pc
Star softening length	4.0	pc
Gas smoothing / softening (minimum)	1.0	pc
$R_{90}^*$ (2D radius enclosing 90% of $M_*$ )	13.3	kpc
$Z_{90}^*$ (height enclosing 90% of $M_*$ )	2.75	kpc
$R_{\text{gas}}$ (defined in Garrison-Kimmel et al. 2018b)	12.1	kpc
$Z_{\text{gas}}$ (defined in Garrison-Kimmel et al. 2018b)	656	pc
scale height of thin stellar disc at $8.2 \pm 0.2$ kpc	380	pc
scale height of thick stellar disc at $8.2 \pm 0.2$ kpc	1240	pc
scale height of cold ( $T < 100\text{K}$ ) gas disc	260	pc
star formation rate at $z = 0$	7.5	$M_\odot/\text{yr}$

**Figure 2.** Mean line-of-sight velocity (top) and velocity dispersion (bottom) maps of the bulge region for stars at a distance from the Sun  $6 < R/\text{kpc} < 10$  in m12m when rescaled to the MW as described in Section 2.1.**Figure 3.** Top: The star formation history of the model. The initial star formation rate is very low but it rises rapidly to a peak at  $\sim 8$  Gyr. Bottom: The metallicity distribution function over the entire galaxy.

The bottom panel of Fig. 3 shows the metallicity distribution function (MDF) across the model. The model's MDF peaks at nearly Solar metallicity and has a long tail to low  $[\text{Fe}/\text{H}]$ . The MDF is similar to some extent to the MDF of the bulge (e.g. Zoccali et al. 2008; Gonzalez et al. 2015).

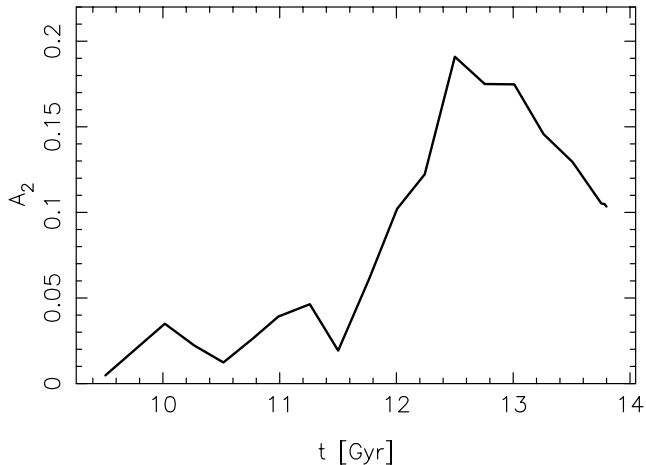


**Figure 4.** Bar amplitude evolution in m12m since redshift  $z = 0.4$  (corresponding to 4.8 Gyr of evolution).

### 3 KINEMATIC FRACTIONATION

Fig. 4 shows the evolution over the last 4.8 Gyr (*i.e.* since redshift  $z = 0.4$ ), of the bar amplitude,  $A_2$ , defined as the usual  $m = 2$  amplitude of the Fourier moment measured over all stars (e.g. Debattista & Sellwood 2000). The bar forms quite late, starting from 11.5 Gyr ( $z \simeq 0.19$ ). It reaches a peak amplitude at  $\sim 12.7$  Gyr, and weakens somewhat in the next Gyr, as is often seen in simulations of isolated galaxies. In isolated simulations, bars generally experience renewed growth past this point (e.g. Combes & Sanders 1981; Sellwood & Moore 1999; Debattista & Sellwood 2000; Bournaud & Combes 2002; O’Neill & Dubinski 2003; Athanassoula 2002; Martinez-Valpuesta et al. 2006), but the late bar formation in this simulation does not give the bar time to strengthen again.

#### 3.1 Density separation

Fig. 5 shows the mass density distribution at  $z = 0$  in face-on and edge-on projections for the model separated by different stellar populations. As in Debattista et al. (2017), younger populations exhibit a stronger bar, and a more prominent box/peanut (B/P) shape, than the older ones. The difference in the B/P strength as a function of age is a signature of kinematic fractionation, as discussed in Debattista et al. (2017).

Fig. 5 also shows the density distribution of the stellar population that was accreted, which we define as stars that formed at radius  $r_f > 40$  kpc. The accreted stars, which account for 4.7% of all the stars, formed primarily ( $> 98\%$ ) by redshift  $z = 1.27$  ( $t_f = 5$  Gyr). They have a density distribution similar to that of the oldest (age  $> 10.8$  Gyr now) in-situ stars, *i.e.* those formed at  $r_f < 40$  kpc (see also El-Badry et al. 2018a). Like the oldest bin, no bar or X-shape is present in the accreted population.

#### 3.2 Age and metallicity dependence of bar amplitude

Fig. 6 shows the dependence of the usual  $m = 2$  Fourier global bar amplitude on the age and metallicity. As also

apparent from the face-on maps in Fig. 5, the bar is stronger in younger populations than in the older ones. The very oldest populations have a quite weak bar overall, while the youngest populations have a  $3.5\times$  stronger bar.

A comparable trend can be seen in the dependence of the bar amplitude on the metallicity. The weakest bar is found in the most metal-poor stars while the most metal-rich stars have the strongest bar. The range of bar amplitudes spanned by the metallicity range is comparable to that spanned by ages, and is continuously varying.

These two trends in the behaviour of bar amplitude are consistent with the results of Debattista et al. (2017) and Buck et al. (2018b).

#### 3.3 Deconstructing the X-shape by age

In the MW, the distance distribution of red clump stars has a single peak at  $|b| \lesssim 5^\circ$  (Babusiaux & Gilmore 2005; Rattenbury et al. 2007; Cao et al. 2013; Gonzalez et al. 2013), becoming bimodal at  $|b| \gtrsim 5^\circ$  (corresponding to  $|Z| \simeq 700$  pc on the minor axis) (McWilliam & Zoccali 2010; Saito et al. 2011; Wegg & Gerhard 2013; Ness et al. 2013). This bimodality is strong in metal-rich stars, but absent in metal-poor stars (Ness et al. 2012; Uttenthaler et al. 2012; Rojas-Arriagada et al. 2014). m12m shows a dependence on  $[\text{Fe}/\text{H}]$ , and also on age (as in Debattista et al. 2017). The present day distributions of star particles of varying ages at different heights are shown in Fig. 7. At  $|Z| < 0.5$  kpc the distributions display only a single peak within the bulge region. At  $0.5 < |Z|/\text{kpc} < 0.75$  stars younger than 4 Gyr ( $t_f = 13.8 - \text{age} > 10$  Gyr) develop a bimodal distribution, whereas distributions of older stars remain unimodal. At  $1.0 < |Z|/\text{kpc} < 1.25$  stars formed at  $8 < t_f/\text{Gyr} < 10$ , which are older than the bar itself, first develop a flat-topped distribution and, above this region, a bimodal one. At  $1.75 < |Z|/\text{kpc} < 2.0$ , the next age bin ( $6 < t_f/\text{Gyr} < 8$ ) develops a flat-topped distribution with hints of a bimodality further from the plane. Stars of yet older ages never develop a bimodality at least within the region where the number of particles is large enough to enable such measurements. The bimodality of older stars appearing at larger heights was predicted by Di Matteo (2016) and Fragkoudi et al. (2017a) from their double disc simulations, but the failure of the oldest stars to exhibit any bimodality to such large heights is a new result.

#### 3.4 Development of an X-shaped metallicity distribution

Fig. 8 shows the evolution from 11 Gyr to 13.8 Gyr of the mean metallicity in three orthogonal projections. At 11 Gyr the bar has not yet developed, and high metallicity stars are mostly concentrated near the mid-plane,  $|Z| < 1$  kpc. At 12 Gyr the bar is forming and an incipient X-shaped ( $\langle [\text{Fe}/\text{H}] \rangle$ ) distribution is evident. Starting near  $X = -5$  kpc the disc can be seen to be bending vertically. Some of this bending continues to 12.8 Gyr by which point the metallicity distribution has a clear X-shape. By 13.8 Gyr the bulge is prominently B/P-shaped and an X-shape in the ( $\langle [\text{Fe}/\text{H}] \rangle$ ) distribution is very apparent. The metallicity distribution is significantly more peanut-shaped than the density distribution, an important prediction of kinematic fractionation

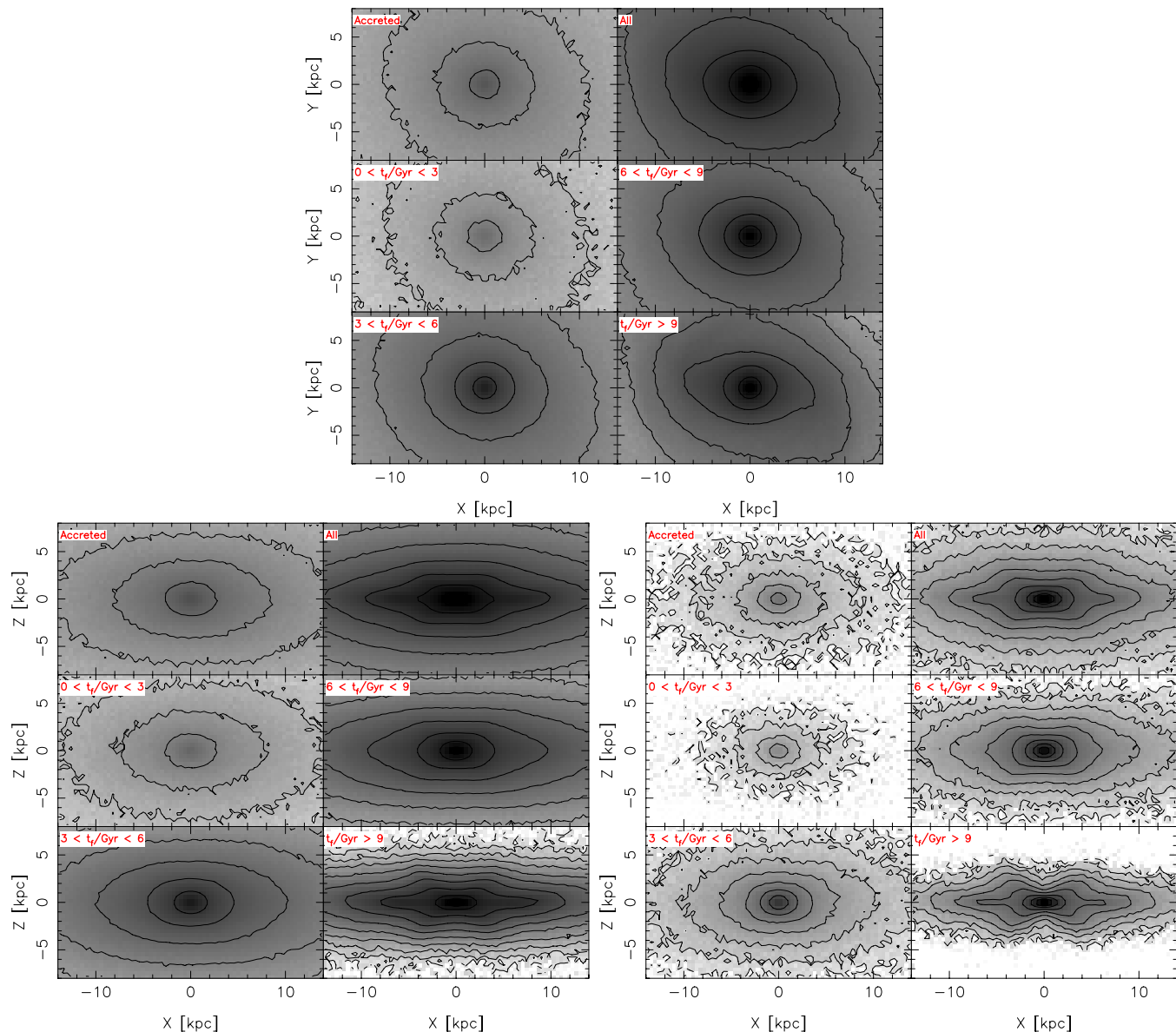


**Figure 5.** Density distributions in the face-on (top panels) and edge-on (bottom panels) projections. The bottom left panels show the full edge-on projection while the bottom right panels show a cross-section with particles chosen within  $|Y| \leq 0.25$  kpc. In the top row of each set of panels we show the accreted stars (left) and all the stars (right). The rest of the panels show populations separated by time of formation of the stars,  $t_f = 13.8$  Gyr-age.

(Debattista et al. 2017) which was confirmed in NGC 4710 (Gonzalez et al. 2017).

#### 4 VERTEX DEVIATION

Because the vertex deviation as a function of metallicity has only been measured reliably in Baade’s Window, at  $(l, b) = (1^\circ, -4^\circ)$ , (Soto et al. 2007; Babusiaux et al. 2010), in this Section we rescale m12m as described in Section 2.1. After rotating the bar to the Solar perspective, we select particles in the equivalent of Baade’s Window in a  $1^\circ \times 1^\circ$  field. This field contains  $\gtrsim 24,000$  star particles within the distance range 6 to 10 kpc. Using these particles, we calculate the

vertex deviation,  $\theta_v$ , defined as:

$$\tan 2\theta_v = \frac{2\sigma_{rl}^2}{|\sigma_r^2 - \sigma_l^2|} \quad (1)$$

where  $\sigma_r^2$  and  $\sigma_l^2$  are the variances of the velocities across the radial and longitudinal directions and  $\sigma_{rl}^2$  is the covariance between the two. The vertex deviation is the angle of the major axis of the velocity ellipsoid with the radial direction.

Radial velocities and proper motions for star particles are calculated from their Galactocentric velocities using *galpy* (Bovy 2015). As did Babusiaux et al. (2010), we only find an insignificant global anisotropy  $\sigma_l/\sigma_r \simeq 1.02$ , reaching to  $\sim 1.07$  for the youngest stars. Our value of  $C_{lr} = \sigma_{rl}^2/(\sigma_r\sigma_l)$ , where  $\sigma_{rl}$  is the covariance, varies from  $\sim -0.25$  for young stars to  $\sim 0.02$  for the oldest ones, a

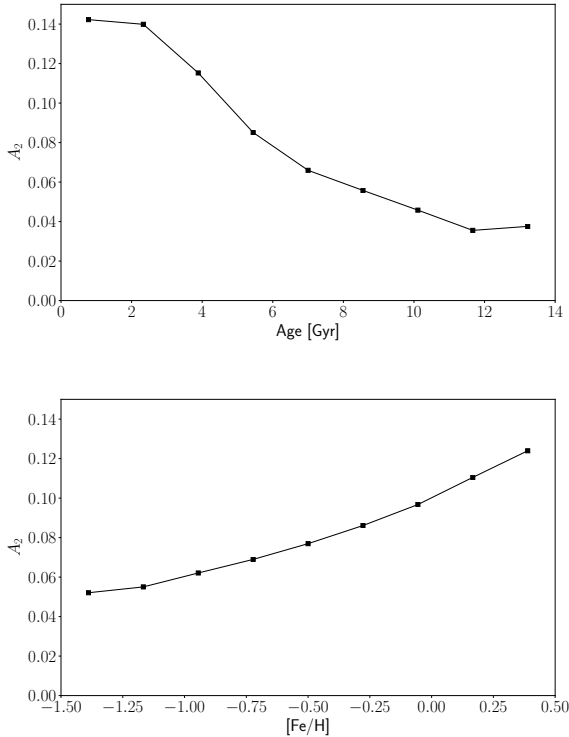


**Figure 6.** Bar amplitude as a function of stellar age (top) and metallicity (bottom) at  $z = 0$ .

decreasing trend found also in the Babusiaux et al. (2010) data. We obtain the corresponding vertex deviation using Eq. 1. Fig. 9 shows  $\theta_v$  as a function of  $[\text{Fe}/\text{H}]$ . While the simulation and the MW do not match in detail, the general trend of decreasing  $|\theta_v|$  for metal-poor stars is reproduced by the simulation. At higher metallicities ( $[\text{Fe}/\text{H}] \gtrsim -0.5$  in the MW, and  $[\text{Fe}/\text{H}] \gtrsim -1$  in m12m), the vertex deviation is roughly constant at  $|\theta_v| \simeq 40^\circ$ . The same trend is also found in the dynamical model of Portail et al. (2017) (their Figure 17).

The vertex deviation  $|\theta_v|$  starts declining at a lower  $[\text{Fe}/\text{H}]$  in the rescaled simulation compared with the MW. The metallicity distribution function in Baade’s window in the simulation is similar to that observed in the MW (Zoccali et al. 2008). However the model’s star formation history, seen in the top panel of Fig 3 is quite different, with star formation peaking later in m12m. This difference in star formation history probably accounts for the difference in the variation of the vertex deviation with metallicity. The constant vertex deviation at the higher metallicities indicates that the relation between line-of-sight and longitudinal velocities is unchanged by the strength of the bar, with only the scatter of the correlation (quantified by  $C_{l,r}$ ) varying.

Debattista et al. (2017) showed that many of the trends with metallicity observed in the MW are fundamentally trends with age, which correlates with metallicity (Bernard et al. 2018). In the top panel of Fig. 10 we plot the vertex deviation as a function of stellar age. The old stars (age  $> 12$  Gyr) exhibit a negligible vertex deviation that increases to  $|\theta_v| \sim 40^\circ$  with decreasing stellar age. The vertex deviation is large for populations as old as 9 Gyr; the bar

therefore is comprised of stellar populations much older than the bar itself. While the star formation history peaks at ages  $\sim 6$  Gyr, we note that the smallest uncertainty in  $|\theta_v|$  is at the youngest stars. The uncertainty therefore represents the scatter in the relation between radial and longitudinal motion, rather than particle number statistics. To test whether an accreted old component is responsible for the observed dependence on age, we measure the vertex deviation for stars that formed in situ, which we now conservatively define as those stars formed at Galactocentric distances smaller than 20 kpc. Fig. 10 shows that old stars formed in situ show a negligible difference from the case when all stars are included, despite the fact that accreted stars are  $\sim 60\%$  of all stars formed before  $t_f = 3$  Gyr. This is similar to the result of El-Badry et al. (2018b) who found the same kinematics for accreted and in-situ stars of the same age. Younger stars also show no significant change when only in-situ stars are chosen, since they dominate at this age. This demonstrates, using a fully cosmological simulation, that the vertex deviation of the velocity ellipsoid of old (metal-poor) stars in the MW’s bulge does not require an accreted bulge component. Nonetheless, the time at which  $\theta_v$  becomes nearly zero is comparable to the time of the last major merger event. Our results therefore do not exclude that it was originally a merger that heated the bulge to produce the trends observed. Indeed m12m has the largest number of satellites of any of the  $\sim 15$  FIRE simulated galaxies in this mass range (Garrison-Kimmel et al. 2018a).

The bottom panel of Fig. 10 shows that before the bar forms no population exhibits a non-zero  $\theta_v$ , as is expected for a stationary, axisymmetric system (e.g. Soto et al. 2007). The presence of the bar therefore drives the vertex deviation; the small  $\theta_v$  in the oldest stars is just a consequence of the weak bar in this population, as seen in Fig. 5.

## 5 CONSTRAINT ON THE AGE OF THE MILKY WAY’S BAR

Sheth et al. (2008) found that the barred fraction amongst high mass galaxies has barely changed since redshift  $z \sim 0.84$ , *i.e.*  $\sim 7$  Gyr ago (see also Erwin 2018). It is important therefore to explore whether the MW’s bar is also this old. Here we show that the ability of the bar to thicken pre-existing populations means that the bar in the MW cannot be young.

Fig. 11 shows the mean age and age dispersion of the model at  $z = 0$  with the model scaled and oriented to the MW. The mean age at large heights,  $|b| \gtrsim 10^\circ$ , is  $\gtrsim 7$  Gyr and decreases slowly to larger heights. Meanwhile the age dispersion is  $\sim 2 - 2.5$  Gyr at these heights. The simulation of Debattista et al. (2017), which formed a bar much earlier in its history, has a comparable mean age at these heights. However the typical age dispersion is lower, 1 Gyr. This suggests that a significant tail of young stars will be found at these large heights in m12m.

Fig. 12 shows the evolution of stellar populations that formed between 5 Gyr and 10 Gyr. The younger populations form the strongest bar, as seen in the density maps of Fig. 5 and Fig. 6. Debattista et al. (2017) attribute this behaviour to the lower radial velocity dispersion of the younger stars at the time of bar formation. The evolution of the average



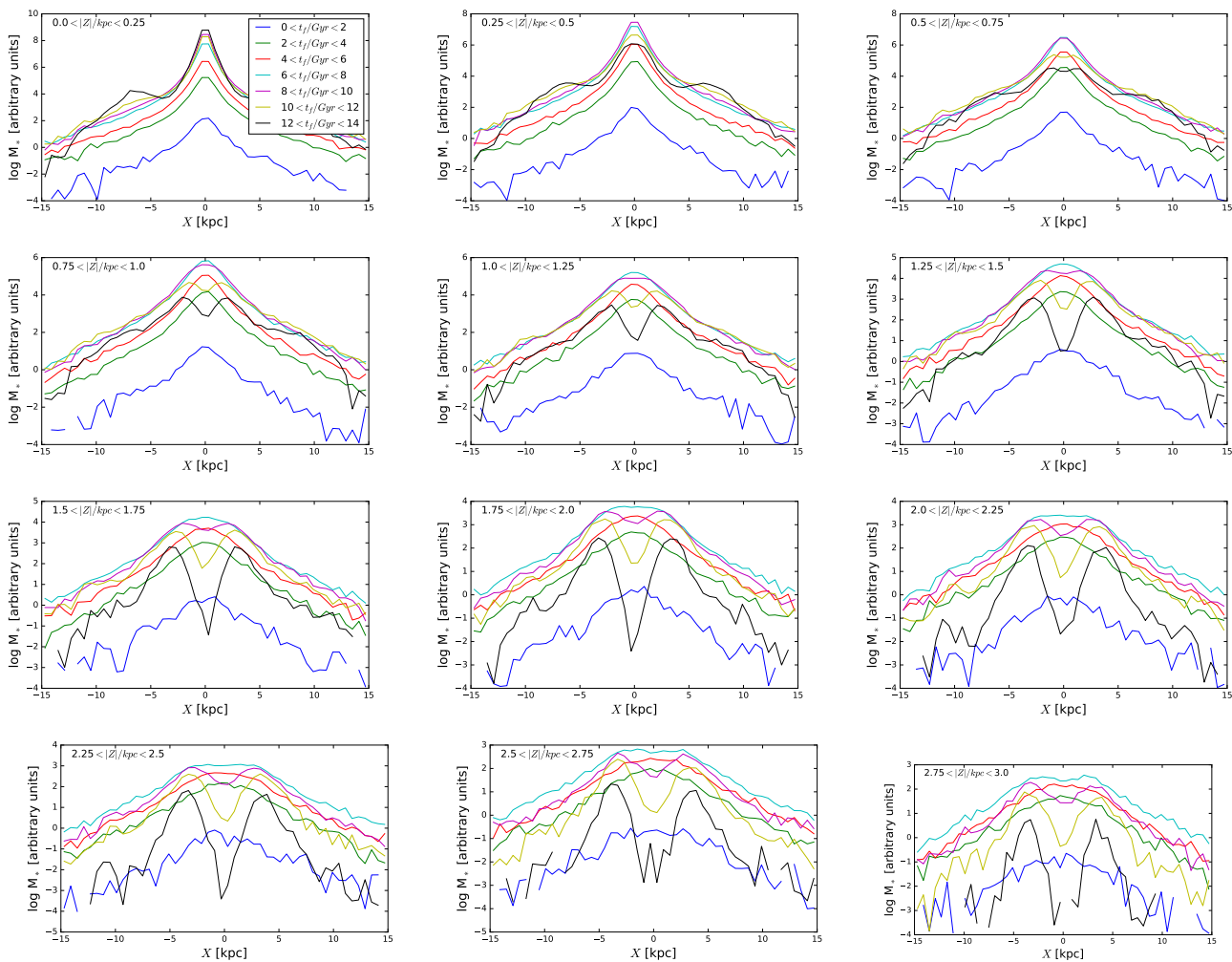


**Figure 7.** Density profiles along the  $X$ -axis (along which the bar is aligned) for different heights above the mid-plane, as indicated. At each height, the profiles are split by the time of formation,  $t_f$ , of the stars, as indicated at top left. The distribution is shown at redshift  $z = 0$ . Only particles at  $|Y| < 0.5$  kpc are included.

heights,  $\langle h_z \rangle$ , averaged in the radial range  $1 < R/\text{kpc} < 6$ , is shown in the bottom panel. The young populations are thinner, as expected (see also Ma et al. 2017). The onset of bar formation between 11 Gyr and 12 Gyr leads to a steepening of the vertical heating of all the populations, but is most prominent for the young populations. Nonetheless, younger populations remain thinner, as required by kinematic fractionation.

The strong vertical heating by the bar dredges relatively young stars into the line of sight of the bulge. With **m12m** scaled as described in Section 2.1, and the bar oriented at  $27^\circ$  to the line of sight to the Galactic centre (Wegg & Gerhard 2013), we map in Fig. 13 the evolution of the fraction of stars that formed during the time interval  $10 \leq t_f/\text{Gyr} \leq 11$  across the bulge, *i.e.* shortly before the bar starts forming. While a negligible fraction of stars this age are found on the minor axis shortly after they form, as the bar strengthens their fraction grows rapidly. Such a fraction of stars that are only 2.8 – 3.8 Gyr old now would be obvious, *particularly* at  $|b| > 8^\circ$ , if it were present in the MW.

Fig. 14 shows the evolution of the fraction of stars of

various ages on the minor axis at  $|b| = 10^\circ$ . The fraction of stars that form after 9 Gyr (which are 4.8 Gyr or younger at present) rises sharply after the bar starts forming. Overall the fraction of stars born after  $t = 10$  Gyr ( $z = 0.34$ ) reaches  $\sim 15\%$ , considerably more than previously suggested in the MW (e.g. Ortolani et al. 1995; Kuijken & Rich 2002; Zoccali et al. 2003; Sahu et al. 2006; Clarkson et al. 2008, 2011; Brown et al. 2010; Valenti et al. 2013; Calamida et al. 2014). Such a fraction of young stars in the bulge has indeed been suggested by recent measurements (Bensby et al. 2017; Haywood et al. 2016; Bernard et al. 2018), but only at low Galactic latitudes ( $|b| < 4^\circ$ ) and at high metallicities. In particular, the age-metallicity relation presented in Bernard et al. (2018) (which is consistent with the microlensed dwarfs from Bensby et al. 2017) shows that young stars are also those in the near-Solar metallicity range ( $-0.2 < [\text{Fe}/\text{H}] < 0.5$ ). This is the dominant population at low latitudes, where the fraction of young stars ( $\sim 15\%$ ) is observed (Haywood et al. 2016), but it weakens with increasing Galactic latitude, and is marginal at  $|b| = 10^\circ$  (Ness et al. 2013; Zoccali et al. 2017). A late-forming bar therefore excessively contaminates

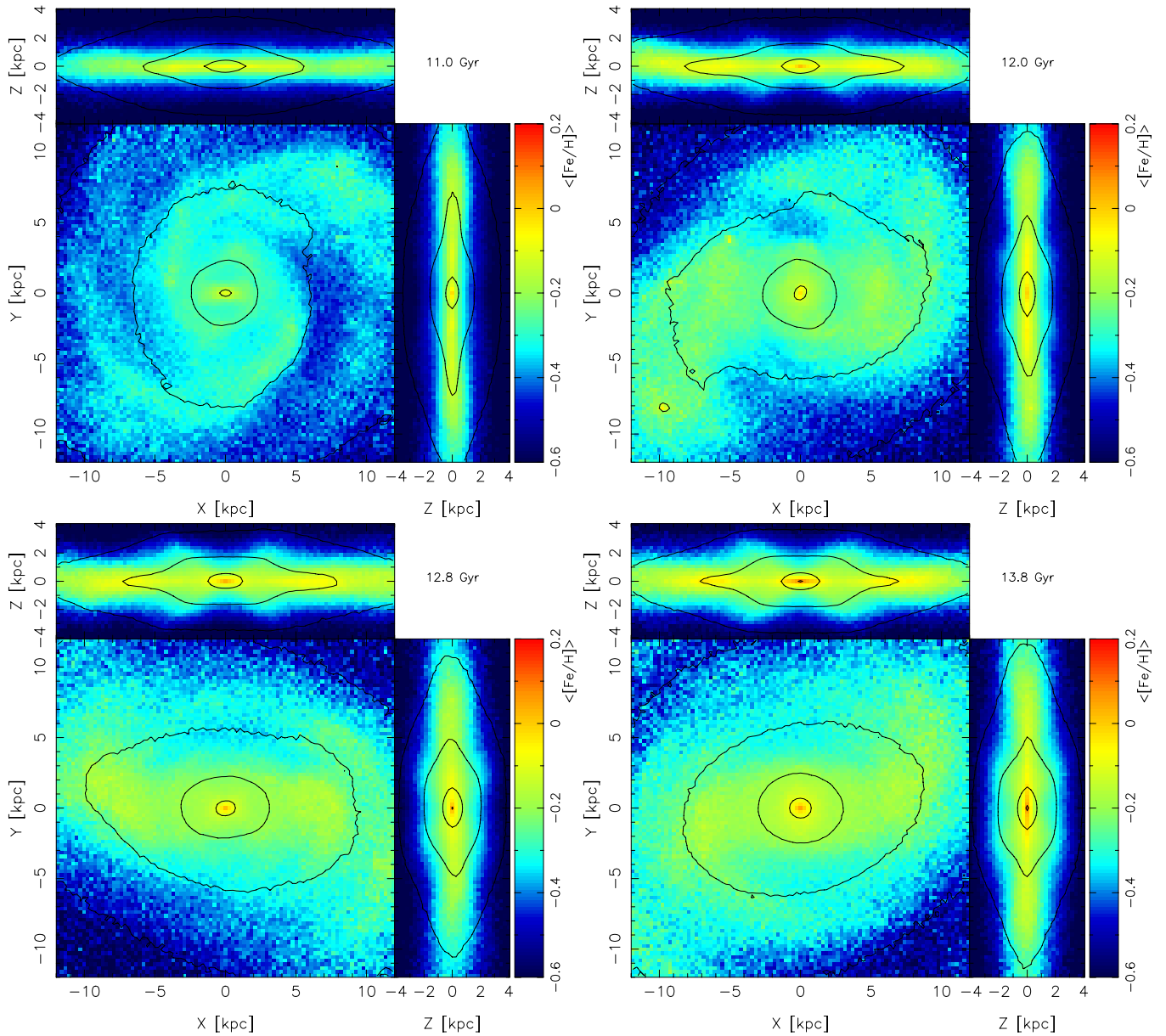


**Figure 8.** Orthogonal projections of the metallicity and density, spanning the formation of the bar. The development of the stellar X-shaped metallicity distribution can be seen in the  $(X, Z)$  projection. The projected surface mass densities are indicated by contours while colours indicate the mean metallicity. The time, indicated at top-right in each set of panels, spans from 11 Gyr ( $z = 0.24$ ) to 13.8 Gyr ( $z = 0$ ), during which time the bar forms.

the bulge with relatively young stars to high latitudes. Stars that form at 10 Gyr are only 1.5 Gyr old by the time the bar starts forming in *m12m*; they are therefore unlikely to have been vertically heated excessively by either physical or numerical effects. The number of them that reach large height therefore is probably a quite robust result that does not depend strongly on the details of the model’s evolution once it is scaled to the size of the MW. Indeed in the model of Debattista et al. (2017), stars forming before the bar are a major component of the bulge at large height. In *m12m*, the star formation drops significantly after 9 Gyr, as seen in Fig. 3; nonetheless 23% of stars are younger than 3.5 Gyr ( $t_f > 10$  Gyr). If this were a factor of  $\sim 2$  lower (e.g. Snaith et al. 2015), the fraction of stars at  $|b| = 10^\circ$  would still be

too high compared to the MW. We conclude that the MW’s bar could not have formed as recently as in *m12m* if the bulge lacks a young population at high latitudes.

## 6 DISCUSSION AND CONCLUSIONS

A non-zero vertex deviation  $\theta_v$  arises once the bar forms. At the low metallicity end the variation in  $\theta_v$  with age (and metallicity) is due to the difference in bar strength that results from populations with different random motions at the time of bar formation. It is in this sense another manifestation of kinematic fractionation, the separation of stellar populations on the basis of their kinematics, rather than

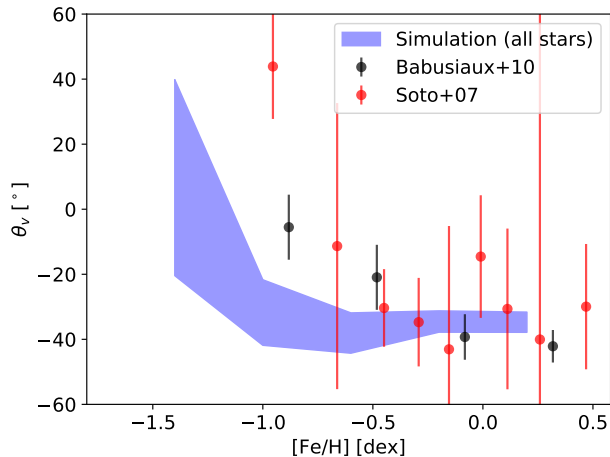


**Figure 9.** Vertex deviation as a function of metallicity for all stars in the rescaled simulation. Points in black are measurements for the MW from Babusiaux et al. (2010) and in red from Soto et al. (2007)

being a signature of an accreted population in the bulge. However an accreted population settles into a hot component and would therefore also produce the same signature, so our results do not exclude an external origin for the zero vertex deviation component in the Milky Way. At the high metallicity end, the vertex deviation is constant, in *m12m* as in the MW, because a strong bar is present. The increasing bar strength with metallicity at this end of the relation is reflected in the decreasing uncertainty on the vertex deviation.

The maximum vertex deviation in *m12m* and the Milky Way are comparable,  $|\theta_v| \sim 40^\circ$ . However  $\theta_v$  in the Milky Way starts decreasing at a larger  $[\text{Fe}/\text{H}]$  than in the model. Since a large  $|\theta_v|$  is possible only if the bar is strong in a particular population, the bar must be strong to lower metallicities in the model than in the Milky Way. In the Milky Way the population of stars at  $[\text{Fe}/\text{H}] \simeq -1$  is dominated by the stellar halo (Ness et al. 2013). The metallicity distribution function of the rescaled *m12m* at Baade’s Window is not much different from that in the Milky Way (Fig. 3). However the star formation peaks at  $\sim 8$  Gyr, which probably accounts for the  $|\theta_v|$  turnoff at lower metallicity in *m12m*. In this sense the vertex deviation may be a quite sensitive probe of the chemical enrichment and dynamical history of the inner disc before the bar formed. This would require measurement of the vertex deviation across a broader part of the bulge to help understand the strength of the bar better.

The long-held view that the bulge is comprised of only old ( $\sim 10$  Gyr old) stars has recently been challenged, starting with the discovery of young to intermediate-age stars in microlensing surveys (Bensby et al. 2011, 2013, 2017). In their simulation, Debattista et al. (2017) showed that the age distribution of stars in the bulge is dominated by old stars, with the fraction of stars between 1 and 4 Gyr old less than 10% everywhere above  $|b| \simeq 5^\circ$ , while the young stars are concentrated towards the mid-plane (Ness et al. 2014). In comparison, *m12m*, the simulation studied in this paper, has

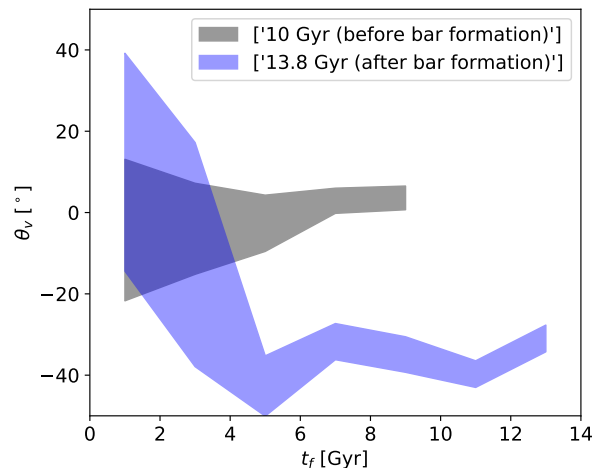
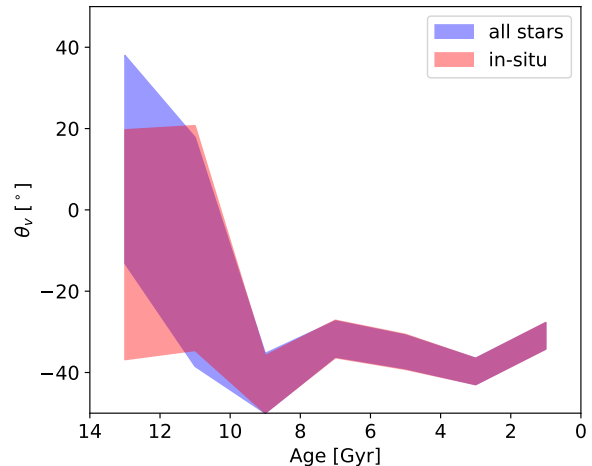


**Figure 10.** Top: Vertex deviation in the rescaled simulation as a function of age. The shaded intervals show  $\theta_v$  for all stars (blue) and stars formed in situ (red). Bottom: Vertex deviation in the rescaled simulation as a function of time of formation of the stars. The blue band is for all stars at  $t = 13.8$  Gyr ( $z = 0$ ) while the grey band is for the simulation before the bar has formed, at  $t = 10$  Gyr ( $z = 0.34$ ) rescaled using the same factor.

$\sim 15\%$  of young to intermediate-age stars all the way up at  $|b| \sim 10^\circ$ . Despite the large differences between the bar formation and star formation histories of these two simulations (and presumably also the MW), the qualitative similarities in their stellar populations on their minor axes provide important information on the time when the bar formed. Indeed the results here and in Debattista et al. (2017) show that stars formed before and during bar formation are efficiently transported to large heights and are therefore likely to be found on the minor axis in significant numbers. A comparison of Fig. 13 here and Fig. 22 of Debattista et al. (2017) reveals that a particularly fruitful place to search for younger populations is at  $l \sim 10^\circ$ , which is most contaminated by them in both simulations; this roughly corresponds to the location of the end of the X-shape on the near-side of the bar. This region has the further benefit that obscura-

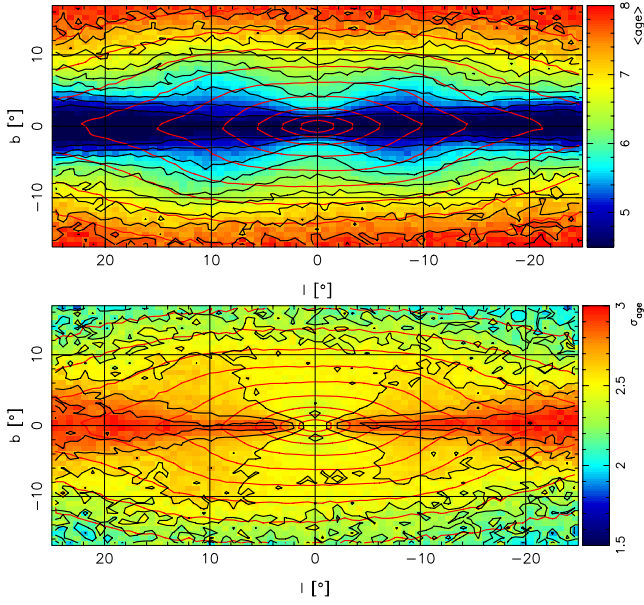


**Figure 11.** Maps in  $(l, b)$  space of the mean age (top) and age dispersion (bottom) at  $z = 0$ , with the model scaled as described in Section 2.1 and oriented to the Sun’s viewing angle. Red contours show the surface density of the model while the black contours are for the plotted quantity.

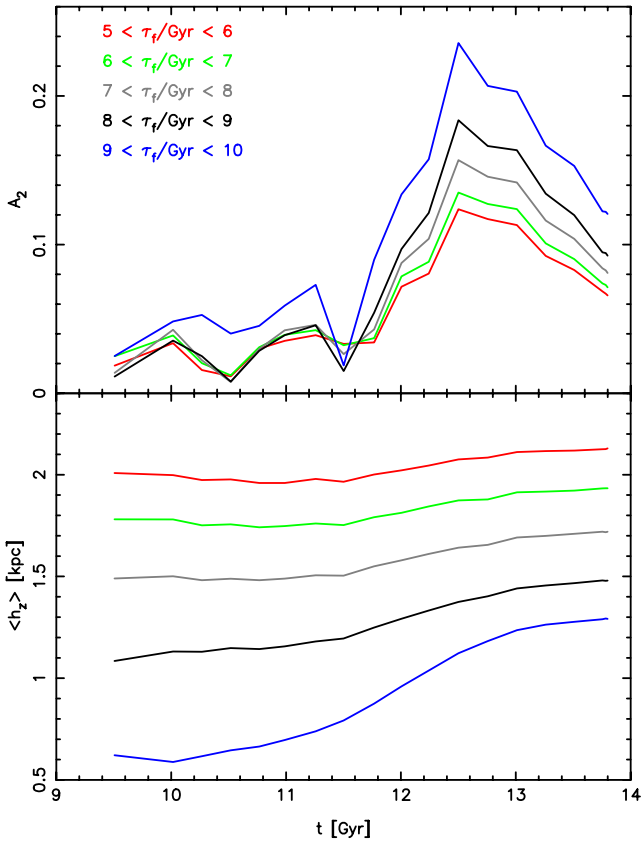


**Figure 12.** The evolution of bar amplitude (top) and average root-mean-square height (bottom) of stars. Stars are separated by time of formation,  $t_f = 13.8 \text{ Gyr} - \text{age}$ . The younger stars form the strongest bar. All populations are vertically heated by the bar.

tion is significantly less severe. A useful strategy would be to compare the age distribution, at fixed latitude, at  $l \sim 10^\circ$  and on the minor axis, which results in a relatively large contrast in the fraction of the younger populations.

## 6.1 Summary

Our results can be summarised as follows:

- We confirm the trends produced by kinematic fractionation. Both the bar strength and the distance bimodality (X-shape) decrease in strength with stellar age. Observed edge-on with the bar side-on the metallicity distribution is more peanut-shaped than the density distribution itself, as observed in NGC 4710. We find that kinematic fractionation occurs in a fully cosmological context (see Section 3) and must therefore have occurred in the Milky Way.
- We find that a non-zero vertex deviation of the velocity ellipsoid at the location of Baade’s Window develops when the bar forms. The vertex deviation varies with metallicity, reaching zero for metal-poor stars, as in the Milky Way. The vertex deviation is a function of age, reaching  $\sim 30 - 40^\circ$  for stars younger than 10 Gyr, but vanishing for stars older than 10 Gyr. As in the MW, the vertex deviation is roughly constant for metal-rich stars ( $[\text{Fe}/\text{H}] \gtrsim -1$  in m12m, and  $[\text{Fe}/\text{H}] \gtrsim -0.5$  in the MW). The vanishing vertex deviation of metal-poor stars is not due to an accreted population of stars, but to the weak bar in the oldest stars, and is also a result of kinematic fractionation (see Section 4).
- A bar forming after redshift  $z = 0.2$  drives a large fraction of stars younger than 4.8 Gyr to large heights on the minor axis of the bulge. Since the fraction of such stars in the Milky Way is negligible at high latitudes, we conclude that its bar is very likely to have formed before this time. The Milky Way’s bar therefore *cannot* be young (see Section 5).

## Acknowledgements.

V.P.D. was supported by STFC Consolidated grant ST/M000877/1. R.E.S. was supported by an NSF Astronomy and Astrophysics Postdoctoral Fellowship under grant AST-1400989. Support for S.G.K. was provided by NASA through Einstein Postdoctoral Fellowship grant PF5-160136 awarded by the Chandra X-ray Center, which is operated by the Smithsonian Astrophysical Observatory for NASA under contract NAS8-03060. A.W. was supported by NASA through grants HST-GO-14734 and HST-AR-15057 from STScI. Support for P.F.H. was provided by an Alfred P. Sloan Research Fellowship, NSF Collaborative Research Grant #1715847 and CAREER grant #1455342. K.E.B. acknowledges support from a Berkeley graduate fellowship, a Hellman award for graduate study, and an NSF Graduate Research Fellowship. Numerical calculations were run on the Caltech compute cluster “Wheeler,” allocations from XSEDE TG-AST130039 and PRAC NSF.1713353 supported by the NSF, NASA HEC SMD-16-7592, and the High Performance Computing at Los Alamos National Labs. CAFG was supported by NSF through grants AST-1412836, AST-1517491, AST-1715216, and CAREER award AST-1652522, by NASA through grant NNX15AB22G, and by a Cottrell Scholar Award from the Research Corporation for Science Advancement.



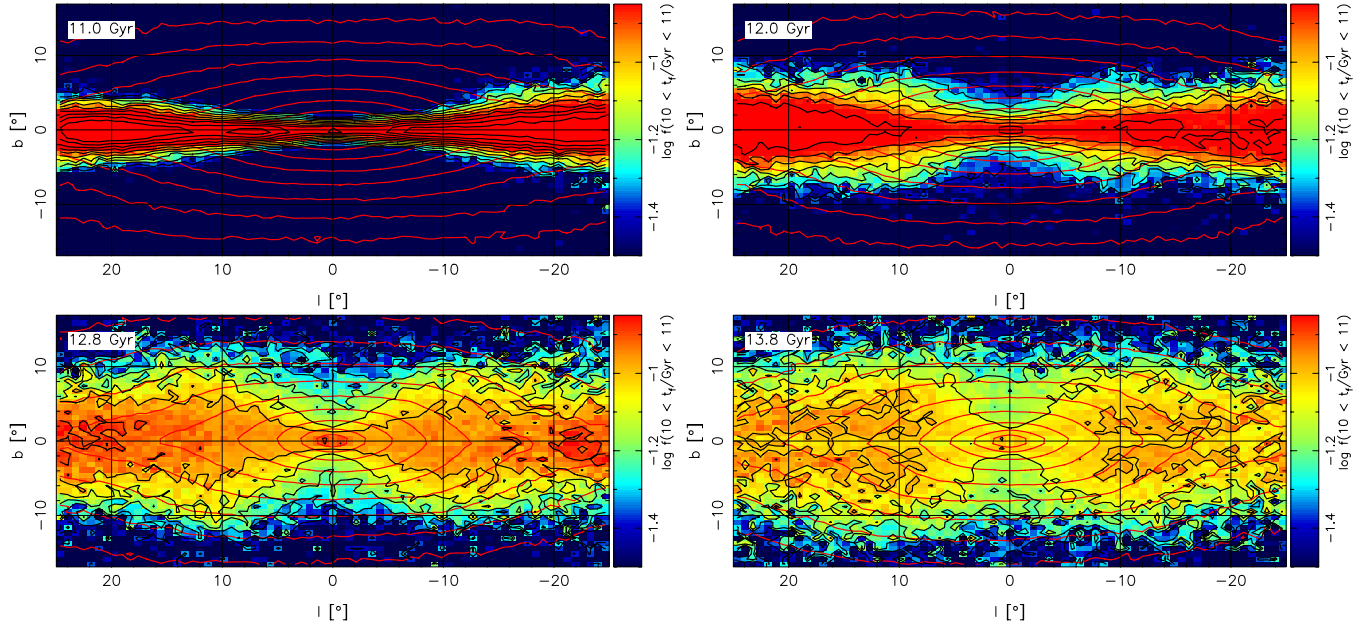


**Figure 13.** Maps of the fraction of stars born in the time interval  $10 \leq t_f / \text{Gyr} \leq 11$ ; the model has been scaled identically at each timestep to approximate the MW’s X-shape at  $z = 0$ , as described in Section 2.1. The snapshots are at 11 Gyr (top left) to 13.8 Gyr (bottom right). Red contours indicate the surface density, as seen from the Solar orientation, which is identical in all panels.

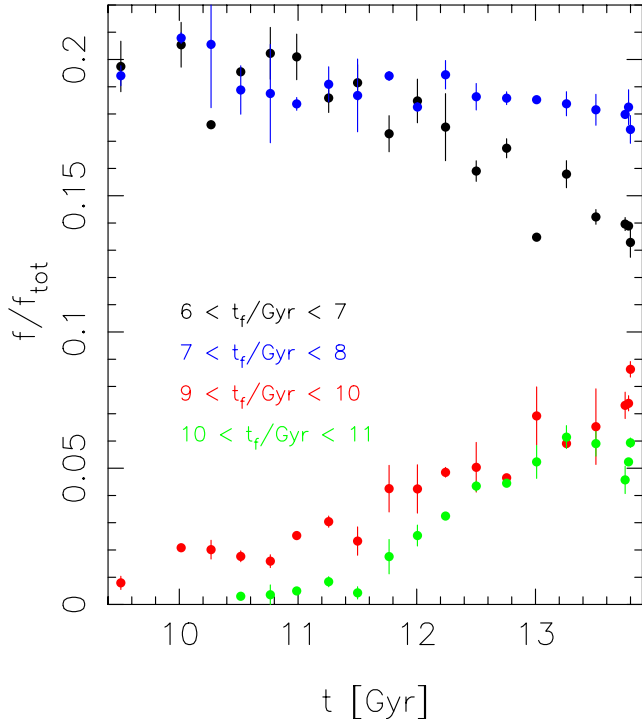


**Figure 14.** The effect of the bar on the evolution of the fraction of the stellar populations at  $|b| = 10^\circ$  on the minor axis in the rescaled version of m12m. Stars are separated by time of formation,  $t_f = 13.8 \text{ Gyr} - \text{age}$ . Each measurement is within a window of  $42'' \times 42''$ . Error bars are based on the difference between  $b = +10^\circ$  and  $b = -10^\circ$ . The bar starts forming at 11.5 Gyr (see Fig. 4).

## REFERENCES

- Aguerri, J. A. L., Balcells, M., & Peletier, R. F. 2001, *A&A*, 367, 428
- Athanassoula, E. 2002, *ApJ*, 569, L83
- Athanassoula, E., Rodionov, S. A., & Prantzos, N. 2017, *MNRAS*, 467, L46
- Aumer, M., & Schönrich, R. 2015, *MNRAS*, 454, 3166
- Babusiaux, C., & Gilmore, G. 2005, *MNRAS*, 358, 1309
- Babusiaux, C., et al. 2010, *A&A*, 519, A77
- Bekki, K., & Tsujimoto, T. 2011, *MNRAS*, 416, L60
- Bensby, T., et al. 2011, *A&A*, 533, A134
- Bensby, T., et al. 2017, *A&A*, 605, A89
- Bensby, T., et al. 2013, *A&A*, 549, A147
- Bernard, E. J., Schultheis, M., Di Matteo, P., Hill, V., Haywood, M., & Calamida, A. 2018, *MNRAS*, 477, 3507
- Binney, J., & Tremaine, S. 2008, *Galactic Dynamics: Second Edition* (Galactic Dynamics: Second Edition, by James Binney and Scott Tremaine. ISBN 978-0-691-13026-2 (HB). Published by Princeton University Press, Princeton, NJ USA, 2008.)
- Bissantz, N., Debattista, V. P., & Gerhard, O. 2004, *ApJ*, 601, L155
- Bland-Hawthorn, J., & Gerhard, O. 2016, *ARAA*, 54, 529
- Bonaca, A., Conroy, C., Wetzell, A., Hopkins, P. F., & Kereš, D. 2017, *ApJ*, 845, 101
- Bonoli, S., Mayer, L., Kazantzidis, S., Madau, P., Bellovary, J., & Governato, F. 2016, *MNRAS*, 459, 2603
- Bournaud, F., & Combes, F. 2002, *A&A*, 392, 83
- Bovy, J. 2015, *ApJS*, 216, 29
- Brown, T. M., et al. 2010, *ApJ*, 725, L19
- Bryan, G. L., & Norman, M. L. 1998, *ApJ*, 495, 80
- Buck, T., Ness, M., Obreja, A., Macciò, A. V., & Dutton, A. A. 2018a, *ArXiv e-prints*
- Buck, T., Ness, M. K., Macciò, A. V., Obreja, A., & Dutton, A. A. 2018b, *ApJ*, 861, 88

- Calamida, A., et al. 2014, *ApJ*, 790, 164
- Cao, L., Mao, S., Nataf, D., Rattenbury, N. J., & Gould, A. 2013, *MNRAS*, 434, 595
- Clarkson, W., et al. 2008, *ApJ*, 684, 1110
- Clarkson, W. I., et al. 2011, *ApJ*, 735, 37
- Combes, F., & Sanders, R. H. 1981, *A&A*, 96, 164
- Debattista, V. P., Ness, M., Gonzalez, O. A., Freeman, K., Zoccali, M., & Minniti, D. 2017, *MNRAS*, 469, 1587
- Debattista, V. P., & Sellwood, J. A. 2000, *ApJ*, 543, 704
- Di Matteo, P. 2016, *PASA*, 33, e027
- Di Matteo, P., et al. 2015, *A&A*, 577, A1
- Di Matteo, P., et al. 2014, *A&A*, 567, A122
- El-Badry, K., et al. 2018a, *MNRAS*, 480, 652
- El-Badry, K., et al. 2018b, *MNRAS*, 473, 1930
- Erwin, P. 2018, *MNRAS*, 474, 5372
- Fiacconi, D., Feldmann, R., & Mayer, L. 2015, *MNRAS*, 446, 1957
- Fragkoudi, F., Di Matteo, P., Haywood, M., Gómez, A., Combes, F., Katz, D., & Semelin, B. 2017a, *A&A*, 606, A47
- Fragkoudi, F., Di Matteo, P., Haywood, M., Khoperskov, S., Gomez, A., Schultheis, M., Combes, F., & Semelin, B. 2017b, *A&A*, 607, L4
- Fragkoudi, F., Di Matteo, P., Haywood, M., Schultheis, M., Khoperskov, S., Gómez, A., & Combes, F. 2018, *A&A*, 616, A180
- Freeman, K., et al. 2013, *MNRAS*, 428, 3660
- Garrison-Kimmel, S., et al. 2018a, arXiv e-prints
- Garrison-Kimmel, S., et al. 2018b, *MNRAS*, 481, 4133
- Gonzalez, O. A., Debattista, V. P., Ness, M., Erwin, P., & Gadotti, D. A. 2017, *MNRAS*, 466, L93
- Gonzalez, O. A., et al. 2016, *A&A*, 591, A7
- Gonzalez, O. A., Rejkuba, M., Zoccali, M., Valent, E., Minniti, D., & Tobar, R. 2013, *A&A*, 552, A110
- Gonzalez, O. A., et al. 2015, *A&A*, 584, A46
- Go, D., Monaco, P., Murante, G., & Curir, A. 2015, *MNRAS*, 447, 1774
- Haywood, M., Di Matteo, P., Snaith, O., & Calamida, A. 2016, *A&A*, 593, A82
- Hopkins, P. F. 2015, *MNRAS*, 450, 53
- Hopkins, P. F., Hernquist, L., Martini, P., Cox, T. J., Robertson, B., Di Matteo, T., & Springel, V. 2005, *ApJ*, 625, L71
- Hopkins, P. F., et al. 2018, *MNRAS*, 480, 800
- Howard, C. D., Rich, R. M., Reitzel, D. B., Koch, A., De Propriis, R., & Zhao, H. 2008, *ApJ*, 688, 1060
- Kraljic, K., Bournaud, F., & Martig, M. 2012, *ApJ*, 757, 60
- Kuijken, K., & Rich, R. M. 2002, *AJ*, 124, 2054
- Leitherer, C., et al. 1999, *ApJS*, 123, 3
- Ma, X., Hopkins, P. F., Wetzel, A. R., Kirby, E. N., Anglés-Alcázar, D., Faucher-Giguère, C.-A., Kereš, D., & Quataert, E. 2017, *MNRAS*, 467, 2430
- Majewski, S. R., et al. 2016, *Astronomische Nachrichten*, 337, 863
- Martinez-Valpuesta, I., & Gerhard, O. 2011, *ApJ*, 734, L20
- Martinez-Valpuesta, I., & Gerhard, O. 2013, *ApJ*, 766, L3
- Martinez-Valpuesta, I., Shlosman, I., & Heller, C. 2006, *ApJ*, 637, 214
- McWilliam, A., & Zoccali, M. 2010, *ApJ*, 724, 1491
- Merritt, D., & Sellwood, J. A. 1994, *ApJ*, 425, 551
- Molaeinezhad, A., Falcón-Barroso, J., Martínez-Valpuesta, I., Khosroshahi, H. G., Balcells, M., & Peletier, R. F. 2016, *MNRAS*, 456, 692
- Ness, M., Debattista, V. P., Bensby, T., Feltzing, S., Roškar, R., Cole, D. R., Johnson, J. A., & Freeman, K. 2014, *ApJ*, 787, L19
- Ness, M., et al. 2013, *MNRAS*, 430, 836
- Ness, M., et al. 2012, *ApJ*, 756, 22
- Ness, M., et al. 2016, *ApJ*, 819, 2
- Noguchi, M. 1999, *ApJ*, 514, 77
- Okamoto, T., Isoe, M., & Habe, A. 2015, *PASJ*, 67, 63
- O'Neill, J. K., & Dubinski, J. 2003, *MNRAS*, 346, 251
- Ortolani, S., Renzini, A., Gilmozzi, R., Marconi, G., Barbuy, B., Bica, E., & Rich, R. M. 1995, *Nature*, 377, 701
- Portail, M., Wegg, C., Gerhard, O., & Martinez-Valpuesta, I. 2015, *MNRAS*, 448, 713
- Portail, M., Wegg, C., Gerhard, O., & Ness, M. 2017, *MNRAS*, 470, 1233
- Qin, Y., Shen, J., Li, Z.-Y., Mao, S., Smith, R. M., M. C. and Rich, Kunder, A., & Liu, C. 2015, *ApJ*, 808, 75
- Rattenbury, N. J., Mao, S., Sumi, T., & Smith, M. C. 2007, *MNRAS*, 378, 1064
- Rojas-Arriagada, A., et al. 2014, *A&A*, 569, A103
- Romano-Díaz, E., Shlosman, I., Heller, C., & Hoffman, Y. 2008, *ApJ*, 687, L13
- Sahu, K. C., et al. 2006, *Nature*, 443, 534
- Saito, R. K., et al. 2012, *A&A*, 537, A107
- Saito, R. K., Zoccali, M., McWilliam, A., Minniti, D., Gonzalez, O. A., & Hill, V. 2011, *AJ*, 142, 76
- Sanderson, R. E., et al. 2018, *ApJ*, 869, 12
- Scannapieco, C., & Athanassoula, E. 2012, *MNRAS*, 425, L10
- Sellwood, J. A., & Moore, E. M. 1999, *ApJ*, 510, 125
- Shen, J., Rich, R. M., Kormendy, J., Howard, C. D., De Propriis, R., & Kunder, A. 2010, *ApJ*, 720, L72
- Sheth, K., et al. 2008, *ApJ*, 675, 1141
- Snaith, O., Haywood, M., Di Matteo, P., Lehnert, M. D., Combes, F., Katz, D., & Gómez, A. 2015, *A&A*, 578, A87
- Soto, M., Rich, R. M., & Kuijken, K. 2007, *ApJ*, 665, L31
- Spinoso, D., Bonoli, S., Dotti, M., Mayer, L., Madau, P., & Bellovary, J. 2017, *MNRAS*, 465, 3729
- Uttenthaler, S., Schultheis, M., Nataf, D. M., Robin, A. C., Lebzelter, T., & Chen, B. 2012, *A&A*, 546, A57
- Valenti, E., Zoccali, M., Renzini, A., Brown, T. M., Gonzalez, O. A., Minniti, D., Debattista, V. P., & Mayer, L. 2013, *A&A*, 559, A98
- Wegg, C., & Gerhard, O. 2013, *MNRAS*, 435, 1874
- Weinberg, M. D. 1985, *MNRAS*, 213, 451
- Wetzel, A. R., Hopkins, P. F., Kim, J.-h., Faucher-Giguère, C.-A., Kereš, D., & Quataert, E. 2016, *ApJ*, 827, L23
- Zana, T., Dotti, M., Capelo, P. R., Bonoli, S., Haardt, F., Mayer, L., & Spinoso, D. 2018, *MNRAS*, 473, 2608
- Zoccali, M., et al. 2014, *A&A*, 562, A66
- Zoccali, M., Hill, V., Lecureur, A., Barbuy, B., Renzini, A., Minniti, D., Gómez, A., & Ortolani, S. 2008, *A&A*, 486, 177
- Zoccali, M., et al. 2003, *A&A*, 399, 931
- Zoccali, M., et al. 2017, *A&A*, 599, A12